

The equilibrium and dynamical cumulants of QCD chiral order parameter with parametric Landau free energy

Lijia Jiang¹, Horst Stöcker², and Jun-Hui Zheng^{1 a}

¹ Institute of Modern Physics, Northwest University, 710127 Xi'an, China

² Frankfurt Institute for Advanced Studies, 60438 Frankfurt am Main, Germany

Received: date / Revised version: date

Abstract. By linearly parameterizing the QCD Landau free energy near the critical point in the baryon chemical potential and temperature plane, we study the fluctuations of the QCD chiral order parameter field (the σ field) in the equilibrium case and dynamical phase transition, respectively. By setting the system size to the typical size of the QGP fireball ($\approx 10^3 \text{ fm}^3$), we show that in the equilibrium case, the discontinuity of the order parameter in the first order phase transition region is replaced by smooth crossover, and the corresponding fluctuations are broadened. Meanwhile, the quartic cumulant κ_4 of the σ field is generally negative near the phase transition line. We further derive the dynamical evolution of the QCD Landau free energy in the Fokker-Plank framework, based on which we deduce the dynamical cumulants of the σ field. Assuming the temperature decreases as a known function of time, we numerically evaluate the dynamical cumulants and confirm that the cumulants present clear memory effects. Moreover, the memory effects on the first order phase transition side is stronger than that on the crossover side, and the dynamical cumulants at the hypothetical freeze-out line present rich non-monotonic structures.

PACS. XX.XX.XX No PACS code given

1 Introduction

The QCD phase structure has been of intensive theoretical and experimental interest for decades [1, 2, 3, 4, 5, 6]. In various extreme conditions, theoretical studies predict different phases of the QCD matter, such as quark-gluon plasma (QGP), hadronic resonance gas (HRG), and color superconductor. Of great interest is the chiral phase transition (χ PT) between the hot QGP phase and the HRG phase [7, 9, 8]. For small baryon chemical potential μ , lattice simulations show that the transition is a broad crossover [10, 11, 12, 13]. For large μ , the sign problem of lattice QCD prevents full *ab initio* simulations. The phenomenological models such as the Nambu-Jona-Lasinio model [14, 15, 16, 17] and quark-meson model [18, 19, 20], and non-perturbative methods like Functional Renormalization Group method [21] and Dyson-Schwinger equation [22, 23] provide relatively complete description on the χ PT, predicting crossover at small μ , first order phase transition at large μ , and the existence of a QCD critical point.

On the other hand, owing to the strong coupling between the chiral σ field and quarks in QCD-inspired models, the high-order cumulants of net-proton production are expected to be sensitive to the increase of fluctuations of the σ field near the critical point [24, 25]. The related observables are being measured by the STAR collaboration at the Relativistic Heavy Ion Collider (RHIC) [26, 27, 28]. The latest experimental data of $\kappa\sigma^2$ for the net-proton production presents a non-monotonic

variation as a function of collision energy for the region $\sqrt{s_{NN}} = 7.7 - 200 \text{ GeV}$ in the Au+Au central collisions [28], which partially agrees with theoretical expectations [24]. However, as shown in Ref. [29], by introducing a freeze-out scheme to the hydrodynamics, the model calculations of the equilibrium critical fluctuations of the net protons still failed to qualitatively explain the full experimental data. It presented the limitation of thermal equilibrium assumption and suggested that the critical dynamics should be taken into account for the description of dynamical χ PT in heavy ion collision.

In recent years, to study the dynamics of non-equilibrium fluctuations, including the dynamical evolution of the order parameter field and the diffusion of the conserved charges, different dynamical models have been developed [30, 31, 32, 33, 34, 35, 36]. The dynamical critical fluctuations consistently present clear memory effects and critical slowing down effects. As a result, both the sign and the magnitude of the high order cumulants can be different from the equilibrium ones, and the kurtosis shows non-monotonic behaviors. To be closer to the experimental process in RHIC, the coupled dynamical evolution of the critical modes and the hydrodynamic background are further developed, like that has been done in the chiral hydrodynamics [37, 38, 39, 40, 41] and hydro+ [42, 43, 44, 45]. Moreover, other kinds of factors such as the spatially nonuniform temperature (and chemical potential) effects on the fluctuations of the order parameter [46], the non-critical fluctuations [47], and the proper freeze-out scheme [29, 48] will also influence the theoretical predictions significantly.

^a e-mail: junhui.zheng@nwu.edu.cn (corresponding author).

As a main component of the critical dynamics, parameterization of the QCD equation of state through the Ising mapping is usually applied to get insight into the universal behaviors in the critical region [49, 50, 51, 52]. However, due to the discontinuities of QCD equation of state on the first order phase transition side, the critical dynamics remains unclear and requires more exploration. In this paper, we focus on the dynamics of critical fluctuations in the χ PT region (including the first order phase transition and crossover) rather than building the complete dynamical modeling. We provide an alternative way to parameterize the QCD Landau free energy in different phase transition scenarios (which also serves as the basis of our discussion on the spatially nonuniform temperature effects in Ising-like models [46]), evaluate the finite size effects of the QCD matter on the order parameter and fluctuations, and develop a distinct set of dynamical equations based on the Fokker-Plank equation to study the dynamical free energy and the dynamical cumulants. The article is structured as following. In Sec. 2, we linearly parameterize the Landau free energy in the (μ, T) plane, where both the crossover and the first order phase transition side are described. In Sec. 3, we set up the parameters in the free energy and present the results of the equilibrium cumulants in the system of different volumes. In Sec. 4, we deduce the dynamical free energy based on the Fokker-Plank equation. In Sec. 5, we numerically calculate the non-equilibrium cumulants at different scenarios and on a hypothetical freeze-out line with a fixed volume $V = 10^3 \text{ fm}^3$. Finally, in Sec. 6, we summarize the main results of this paper and give a discussion.

2 Parameterization of the free energy

Because the critical behaviors of the σ field fall into the same universality class as the 3D Ising model [53], in principle, one can parameterize the QCD equation of state by directly mapping the QCD parameters (μ, T) to the Ising variables (r, h) , as is done in Refs. [54, 55, 56, 57]. Combined with the dynamical models, there are various interesting dynamical effects presented, like memory effects and universal off-equilibrium scaling behaviors [55, 31, 58, 36]. However, the early studies focus their discussions of critical dynamics on the crossover side, due to the discontinuities of the equations of state in the first order phase transition region. In this section, we develop an alternative method to directly parameterize the QCD free energy, in which the two phase transition scenarios are unified in a same framework.

According to the Landau theory of phase transition, the free energy in the critical region is supposed to be analytic and obeys the symmetry of the Hamiltonian. Then, the Landau free energy density of the χ PT [59, 60] can be generally written in terms of the σ field as

$$\mathcal{Q}[\sigma] = \alpha_1(\mu, T)\sigma + \frac{\alpha_2(\mu, T)}{2}\sigma^2 + \frac{\alpha_3(\mu, T)}{3}\sigma^3 + \frac{\alpha_4(\mu, T)}{4}\sigma^4, \quad (1)$$

which is Taylor expanded as a function of σ up to the fourth order. The constant term is omitted because it is irrelevant to the structure of the QCD phase diagram. Note that a zero-momentum mode approximation of the σ field is assumed in above, be-

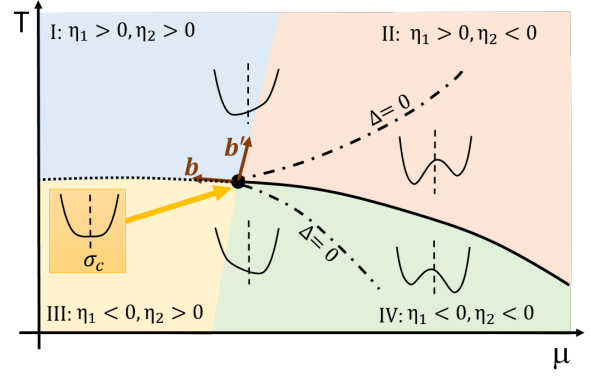


Fig. 1: A sketch of the QCD phase diagram. The colored 4 zones (I-IV) are sorted according to the sign of η_1 and η_2 . The dash-dotted lines determined by $\Delta \equiv (\frac{\eta_1}{2\eta_4})^2 + (\frac{\eta_2}{3\eta_4})^3 = 0$, are the boundary of the region where two local minima coexist in the free energy.

cause we focus on the phase transition region in the vicinity of the critical point, where the long-wavelength modes are dominant. The distribution of the critical field is described by the probability distribution function $P[\sigma] \propto \exp\{-\mathcal{Q}[\sigma]V/T\}$ [24], where V is the volume of the system. In the chiral limit, $\alpha_1 = \alpha_3 = 0$, while for the physical world, a finite $\alpha_1\sigma$ term is introduced to handle the explicit chiral symmetry breaking of the quark masses [61]. The cubic term, $\alpha_3\sigma^3$, emerges after the renormalization contributed from the high-momentum modes of the σ field. The coefficient of the quartic term, α_4 , is supposed to be positive, in order to sustain the stability of the system.

In the thermodynamic limit ($V \rightarrow \infty$), the phase structure is fully determined by the global minimum of the free energy (1). It is convenient to present the information of the χ PT by performing a translation transformation for the σ field in the free energy, i.e., $\sigma = \tilde{\sigma} + \sigma_c$, where

$$\sigma_c(\mu, T) = -\frac{\alpha_3(\mu, T)}{3\alpha_4(\mu, T)}. \quad (2)$$

Consequently, the cubic term in Eq. (1) can be eliminated, and we obtain the translated free energy density (after getting rid of a constant term)

$$\mathcal{Q}[\tilde{\sigma}] = \eta_1(\mu, T)\tilde{\sigma} + \frac{1}{2}\eta_2(\mu, T)\tilde{\sigma}^2 + \frac{1}{4}\eta_4(\mu, T)\tilde{\sigma}^4, \quad (3)$$

which has exactly the same form as the free energy density of the Ising model. The redefined coefficients, η_i , can be expressed as functions of the original coefficients α_i and the shift σ_c by

$$\eta_1 = \alpha_1 + \alpha_2\sigma_c - 2\alpha_4\sigma_c^3, \quad (4)$$

$$\eta_2 = \alpha_2 - 3\alpha_4\sigma_c^2, \quad (5)$$

$$\eta_4 = \alpha_4. \quad (6)$$

Now the $\tilde{\sigma}$ field has become an effective order parameter, which behaves just like the spin density in the Ising model.

With the translated free energy, we can divide the phase spaces in the μ - T plane into four zones, according barely to the

sign of η_1 and η_2 . As shown in Fig. 1, the phase transition line is determined by $\eta_1 = 0$, and the order of the phase transition is determined by the sign of η_2 . At the right part of the diagram (zone II and IV), $\eta_2 < 0$, the phase transition is first order, as there is a coexistence region around the phase transition line, in which two local minima of the free energy coexist. The coexistence region is separated out by the dash-dotted lines, which are determined by $\Delta \equiv (\frac{\eta_1}{2\eta_4})^2 + (\frac{\eta_2}{3\eta_4})^3 < 0$. The physical vacuum locates at the lower minimum of the free energy. This is the typical feature of the first order phase transition. For the other parts of the μ - T plane where $\Delta > 0$, only one minimum exists, and the system undergoes a continuous phase transition (crossover) as η_1 crosses its zero point. The sign of η_1 determines the location of the global minimum. In general, in the upper regions (zone I and II), with $\eta_1 > 0$, the global minimum is at $\tilde{\sigma} < 0$ (i.e. $\sigma < \sigma_c$); while in the lower regions (zone III and IV), with $\eta_1 < 0$, the global minimum is at $\tilde{\sigma} > 0$ (i.e. $\sigma > \sigma_c$). At the critical point (μ_c, T_c) , both η_1 and η_2 vanish.

To parameterize the coefficients in $\Omega[\tilde{\sigma}]$ linearly, it is convenient to define two unit vectors $\mathbf{b} = (\cos \theta_b, \sin \theta_b)$ and $\mathbf{b}' = (\cos \theta_{b'}, \sin \theta_{b'})$ in the μ - T plane. The vector \mathbf{b} is parallel to the tangent of the phase transition curve at the critical point; The vector \mathbf{b}' is along the boundary of region I and II in Fig. 1. Note that \mathbf{b} and \mathbf{b}' are not necessarily orthogonal. The angle between them are determined by the realistic QCD equation of state around the critical point, which is still under study. By projecting the vector $(\mu - \mu_c, T - T_c)$ onto the perpendicular vector of \mathbf{b} and that of \mathbf{b}' , respectively, the coefficients are linearly parameterized as:

$$\eta_1(\mu, T) = d_1[(\mu - \mu_c) \sin \theta_b - (T - T_c) \cos \theta_b], \quad (7)$$

$$\eta_2(\mu, T) = d_2[-(\mu - \mu_c) \sin \theta_{b'} + (T - T_c) \cos \theta_{b'}], \quad (8)$$

$$\eta_4(\mu, T) = d_4. \quad (9)$$

With these projections, the sign of η_1 and η_2 at different parts (I-IV) can be correctly expressed by simply constraining all the constants to $d_i > 0$ ($i = 1, 2, 4$), i.e., in the right side of the vector \mathbf{b} , $\eta_1 > 0$, and in the left side of \mathbf{b}' , $\eta_2 > 0$. Note that the magnitude of d_i are again determined by the QCD equation of state, which currently remains unknown. In the following, for simplicity and illustration, we treat them as input parameters, and make qualitative calculations and discussions. Along the phase transition curve, $\eta_1(\mu, T) = 0$, the correlation length is $\xi = \eta_2^{-1/2}$ on the crossover side and $\xi = (-2\eta_2)^{-1/2}$ on the first order phase transition side, which diverges at the critical point where $\eta_2 = 0$ [4]. In the critical region, we assume that the change of σ_c on the phase transition line is small and treat the variable $\sigma_c(\mu, T)$ as a constant, $\sigma_c(\mu, T) = \sigma_c(\mu_c, T_c)$, in the zero-order approximation of variables $\mu - \mu_c$ and $T - T_c$. Then, the translated free energy density (3) is fully parameterized by $\mu_c, T_c, \sigma_c, d_1, d_2, d_4, \theta_b$, and $\theta_{b'}$. By using the relations Eq. (2) and Eqs. (4)-(6), the original free energy $\Omega[\sigma]$ (Eq.(1)) can also be expressed in the parameterized form.

Through the transformation from Eq. (1) to Eq. (3) and the parameterization Eqs. (7)-(9), we have built the connection between the QCD free energy and the Ising free energy at the mean-field level. Indeed, Eqs. (7) and (8) describe the dependence of η_1 and η_2 on the QCD variables (μ, T) in the linear approximation, and the coefficients η_1 and η_2 in the translated

free energy (Eq. (3)) are directly related to the reduced magnetic field and temperature h and r in the Ising model, respectively. Note that the current parameterization of the QCD free energy is only up to the linear order, which works in the region close to the critical point. When treating a larger region in the μ - T plane, higher order expansions of $\mu - \mu_c$, and $T - T_c$ should be taken into account. It is worth stressing that this parameterization can also be applied to the (hadronic) gas-liquid phase transition [62,63] or to other similar scenarios, as long as they belong to the same universality class. With this parametric free energy, we can easily develop approaches to study the equilibrium and non-equilibrium cumulants in different phase transition scenarios, as will be shown in the following sections.

3 parameter setup and equilibrium cumulants

In this section, we calculate the equilibrium cumulants based on the above parametric Landau free energy. The cumulants of the σ field are defined as

$$\kappa_1 = \mu_1, \quad (10)$$

$$\kappa_2 = \mu_2 - \mu_1^2, \quad (11)$$

$$\kappa_3 = \mu_3 - 3\mu_2\mu_1 + 2\mu_1^3, \quad (12)$$

$$\kappa_4 = \mu_4 - 4\mu_3\mu_1 - 3\mu_2^2 + 12\mu_2\mu_1^2 - 6\mu_1^4, \quad (13)$$

where the moments μ_n are

$$\mu_n = \langle \sigma^n \rangle = \int d\sigma \sigma^n P[\sigma] / \int d\sigma P[\sigma], \quad (14)$$

and the probability distribution function for the σ field is

$$P[\sigma] \propto \exp\{-\Omega[\sigma]V/T\}. \quad (15)$$

The numerical calculation of the cumulants are implemented with the following setup of parameters: $(\mu_c, T_c) = (240, 170)$ MeV, $\sigma_c = 50$ MeV, $d_1 = 3 \times 10^4$ MeV², $d_2 = 400$ MeV, $d_4 = 15$, $\sin \theta_{b'} = -\cos \theta_b = 0.99$, and $\cos \theta_{b'} = \sin \theta_b = 0.141$. Here, $\mathbf{b} \perp \mathbf{b}'$ is set for simplicity. The choice of these parameters are constrained by comparing with the effective potential and cumulants from the linear sigma model with constituent quarks in [37], with which the equilibrium values of the cumulants in the phase transition region are approximately of the order $\kappa_n \sim 10^n$ MeVⁿ.

Note that the discussion and parameterizations of the free energy density (1) in above is in the thermodynamic limit. In reality, especially in the experimental environment, the size of the QGP fireball in the heavy ion collision is finite (the typical volume of the fireball is approximately $V = 10^3$ fm³). The finite size has a direct influence on the renormalization process. Consequently, the coefficients α_i in Eq. (1) depend on the volume, and further, the parameters $\mu_c, T_c, \sigma_c, d_1, d_2, d_4, \theta_b$, and $\theta_{b'}$ are also volume-dependent. There is a standard process for the renormalization of the coefficients of the free energy [64]. However, even through the volume will change the magnitude of the parameters, the parameterized form of the Landau free energy density will not be changed. Therefore, in this article, we will not discuss the finite size corrections to the free energy density itself but simply utilize the same parameter set for different volumes to study the behaviors of the cumulants.

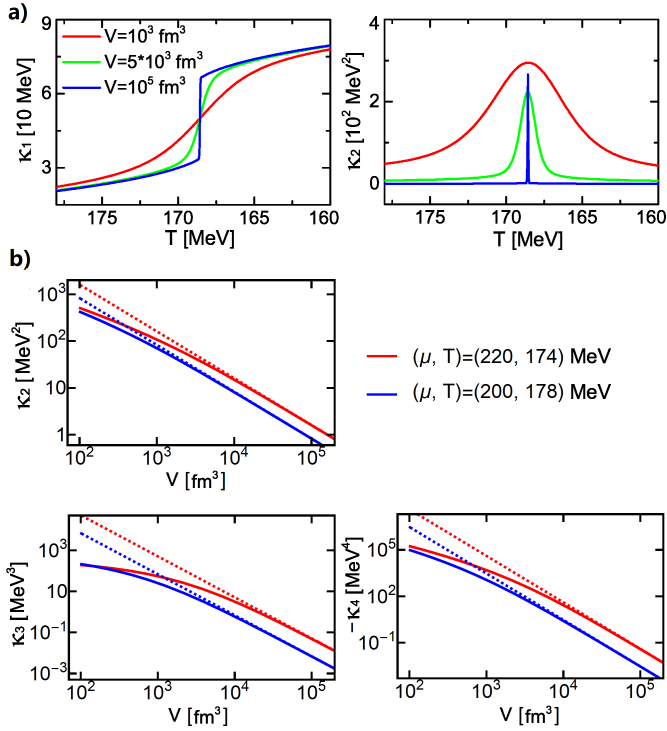


Fig. 2: (a) The cumulants κ_1 and κ_2 of the σ field as functions of the temperature with different fixed volumes in the first order phase transition regime. The chemical potential is fixed at $\mu = 250 \text{ MeV}$. (b) The κ_2 , κ_3 and κ_4 as functions of volume in the crossover regime. The solid lines are given by Eq.(11)-(13). The dotted lines represent fluctuations determined by the Gaussian approximation, $\tilde{\kappa}_2 = T\xi^2/V$, and the perturbative results $\tilde{\kappa}_3$ and $\tilde{\kappa}_4$ [31].

Even without considering the influence on the free energy density from the renormalization of size, we still have to face the finite-volume effects on the fluctuations of the σ field as shown in the probability function (15). In Fig. 2(a), we present the first two order cumulants of the σ field with respect to temperature for different volumes. The chemical potential is fixed at $\mu = 250 \text{ MeV}$ so the system undergoes a first order phase transition as the change of temperature. For a large enough volume (say 10^5 fm^3), the expectation value $\kappa_1 = \langle \sigma \rangle$ is discontinuous because the barrier of the free energy ($\Delta\Omega V$) can not be overcome by the thermodynamic fluctuations, i.e., $\Delta\Omega V \gg T$. The σ field locates only near the global minimum point and the variance κ_2 is also suppressed by the volume. Specifically, on the phase transition line $\eta_1 = 0$, the correlation length of the σ field is $\xi = (-2\eta_2)^{-1/2}$ and the barrier is $\Delta\Omega V = \eta_2^2 V / 4\eta_4$. Thus, the discontinuity of the first order phase transition becomes evident when $V \gg 16T\eta_4\xi^4$. For a smaller system volume, the value of T/V in the probability distribution function $P[\sigma]$ grows. As a result, in the first order phase transition region, the σ field is allowed to be at both of the local minimum points of the free energy with considerable probability, which leads to the enhancements of variance κ_2 . Meanwhile, the expectation value κ_1 deviates from the global minimum of the free energy, and its discontinuity is rounded. Similar finite-size

rounding effects of a first order phase transition can also be found in Refs.[65,66,67]. This hints that for a small system, the perturbation theory around the global minimum does not work well anymore, and the equation of states obtained in the thermodynamic limit [24,31] are not suitable for the system with small size.

In Fig. 2(b), we also plot $\kappa_2 - \kappa_4$ as functions of the volume of the system for (T, μ) locating in the crossover regime, and make comparisons with the Gaussian fluctuations $\tilde{\kappa}_2 = T\xi^2/V$ and the perturbative non-Gaussian cumulants $\tilde{\kappa}_3 = -2\lambda_3(T/V)^2\xi^6$ and $\tilde{\kappa}_4 = 6(T/V)^3[2(\lambda_3\xi)^2 - \lambda_4]\xi^8$ [31]. For large volume, the variance κ_2 is consistent with $\tilde{\kappa}_2$. But as the decreasing of the volume, the non-Gaussian corrections are enhanced as the widening of the variance, and lead to a significant deviation of κ_2 from $\tilde{\kappa}_2$. The Gaussian approximation is valid when the non-Gaussian contributions are small. Expanding Eq. (3) around the extreme point $\tilde{\sigma}_m$ where $\partial_{\tilde{\sigma}}\Omega = 0$, the third and forth order coupling constants of the fluctuation $\delta\tilde{\sigma}$ defined as in Refs. [24, 31] become $\lambda_3 = 3\eta_4\tilde{\sigma}_m$ and $\lambda_4 = \eta_4$. The corresponding conditions for the validity of the Gaussian approximation are $\lambda_3(\delta\tilde{\sigma})^3 V / 3T \ll 1$ and $\lambda_4(\delta\tilde{\sigma})^4 V / 4T \ll 1$. The typical magnitude of $\delta\tilde{\sigma}$ is of the order of $\sqrt{\tilde{\kappa}_2}$. Thus, the conditions become $V \gg (\eta_4\tilde{\sigma}_m)^2\xi^6 T$ and $V \gg \eta_4\xi^4 T / 4$. Specially on the phase transition line $\eta_1 = 0$, we have $\tilde{\sigma}_m = 0$ and the first condition is satisfied automatically. In the condition of large volume, the higher order cumulants κ_3 and κ_4 also become consistent with the perturbative results as shown in the figure.

In the following calculations, we fix the system volume to the typical size of the QGP fireball, $V = 10^3 \text{ fm}^3$. In Fig. 3, we present the density plots of the equilibrium cumulants $\kappa_2 - \kappa_4$ in the $\eta_1 - \eta_2$ plane. The magnitude of κ_2 , κ_3 , and κ_4 in the first order phase transition region ($\eta_2 < 0$) are generally larger than that in the crossover region ($\eta_2 > 0$) for a given small η_1 . Similar to Ref. [24], κ_3 changes its sign after crossing the phase transition line. On the other hand, unlike the results in Ref. [24], κ_4 is generally negative (red color region) near the phase transition line ($\eta_1 = 0$), for both the crossover side and the first order phase transition side. The change of sign for κ_4 happens at the dotted blue lines, inside which the red color region is much larger than the region rounded up by the dashed purple lines (refers to the sign-change line of κ_4 in the thermodynamic limit). As explained in the above paragraphs, the broadening of the negative κ_4 region on the first order phase transition side is due to the rounding effects, since the two-peak shape of $P[\sigma]$ (for the double-well of $\Omega[\sigma]$ with small volume) has less kurtosis than the Gaussian distribution [57]. While in the thermodynamic limit for the first order phase transition region, even through the free energy $\Omega[\sigma]$ also has the double-well shape, one peak of $P[\sigma]$ is strongly enhanced by the large volume comparing to the other one, thus $P[\sigma]$ shapes like a one-peak distribution and only the region near the global minimum of $\Omega[\sigma]$ is distributed. As a result, κ_4 is negative only in the crossover region in the thermodynamic limit [57], striking contrast to the results in systems of small size.

4 Dynamical equations for the free energy

In this section, we employ the Fokker-Plank equation to study the dynamical behaviors of the parameterized QCD free en-

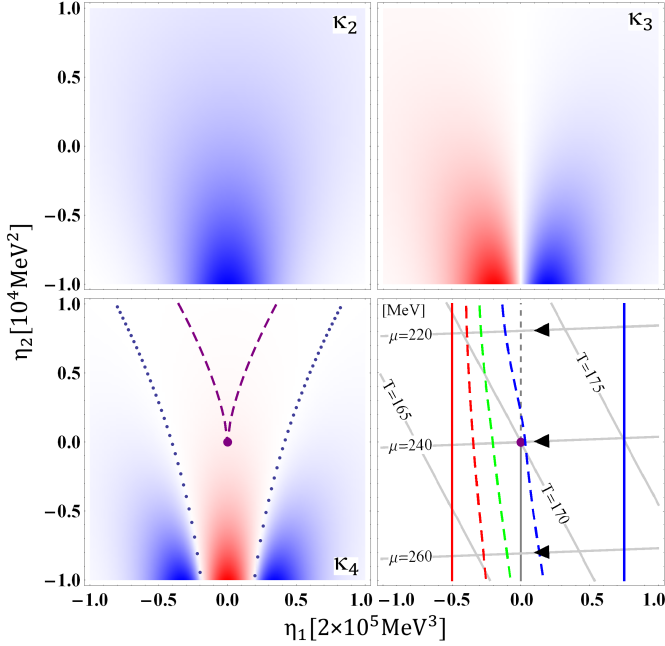


Fig. 3: The equilibrium cumulants $\kappa_2 - \kappa_4$ in the η_1 - η_2 plane for $V = 10^3 \text{ fm}^3$. The colors red and blue refer to negative and positive sign of the cumulants, respectively, and darker colors correspond to larger magnitudes of the cumulants. $\eta_2 < 0$ corresponds to the first order phase transition region and $\eta_2 > 0$ corresponds to the crossover region. $\eta_1 = 0$ refers to the phase transition line. In the subfigure κ_4 , the dotted blue lines mark the boundary where κ_4 changes the sign; while as a comparison, the dashed purple lines are the boundary in the thermodynamic limit case. The bottom-right subfigure shows the setup of the dynamical evolution in Sec. 5, and visualize the memory effects with different relaxation rates. The grey lines are the contours of μ and T in the η_1 - η_2 plane. The dynamical evolution are set to be along fixed chemical potentials, while the blue and red solid line are the starting and hypothetical freeze-out line for the dynamical evolution. The evolution direction is marked by arrows. The dashed red (green, blue) line, on which the equilibrium κ_1 equals to the dynamical κ_1 on the solid red line (hypothetical freeze-out line) with relaxation rate $\tau_{\text{rel}} = 0.05(0.1, 0.2 \text{ fm})$, represents the effective freeze-out line due to the memory effects of dynamics.

ergy. The Fokker-Plank equation for the dynamical probability distribution (denoted by $P[\sigma; t]$) of the σ field is [31]

$$\partial_t P[\sigma; t] = -\frac{1}{m_\sigma^2 \tau_{\text{eff}}} \partial_\sigma \{ \partial_\sigma (\Omega[\sigma; t] - \Omega_0[\sigma]) P[\sigma; t] \}, \quad (16)$$

where $\Omega[\sigma; t] \equiv -\frac{T}{V} \ln P[\sigma; t]$ is the dynamical free energy density and $\Omega_0[\sigma]$ is the equilibrium free energy density at the point $(\mu(t), T(t))$ (see Eq. (1)). The parameter τ_{eff} is the effective relaxation rate. m_σ is the equilibrium mass of the σ field, which is defined as

$$m_\sigma^2 = \frac{d^2 \Omega_0[\sigma]}{d\sigma^2} \Big|_{\sigma=\sigma_0}, \quad (17)$$

where σ_0 is the global minimum of $\Omega_0[\sigma]$. The following calculation assumes that the dependence of the relaxation rate τ_{eff} on the equilibrium correlation length $\xi_{\text{eq}}(\mu, T)$ satisfies

$$\tau_{\text{eff}} = \tau_{\text{rel}} \left(\frac{\xi_{\text{eq}}}{\xi_{\text{ini}}} \right)^z, \quad (18)$$

where $\xi_{\text{eq}} = m_\sigma^{-1}$ [31]. Here τ_{rel} and ξ_{ini} are the initial relaxation rate and the initial equilibrium correlation length, respectively. The value $z = 3$ is given by the dynamical critical exponent of Model H [68, 69].

The time evolution equation of $\Omega[\sigma; t]$ is deduced from Eq. (16), and we obtain

$$\begin{aligned} \partial_t \Omega[\sigma; t] = & \Omega[\sigma; t] \partial_t \left(\ln \frac{T}{V} \right) + \frac{T}{V} \frac{\partial_\sigma^2 (\Omega[\sigma; t] - \Omega_0[\sigma])}{m_\sigma^2 \tau_{\text{eff}}} \\ & - \frac{\partial_\sigma (\Omega[\sigma; t] - \Omega_0[\sigma]) \partial_\sigma \Omega[\sigma; t]}{m_\sigma^2 \tau_{\text{eff}}}. \end{aligned} \quad (19)$$

By denoting $\Omega[\sigma; t] = \sum_i \alpha_i(t) \sigma^i / i$, the time evolution of the coefficient $\alpha_i(t)$ becomes,

$$\begin{aligned} \frac{d\alpha_i(t)}{dt} = & \alpha_i(t) \partial_t \left(\ln \frac{T}{V} \right) + \frac{i(i+1)T}{V} \frac{[\alpha_{i+2}(t) - \alpha_{i+2}^0]}{m_\sigma^2 \tau_{\text{eff}}} \\ & - \sum_{j=0}^i \frac{i\alpha_{i-j+1}(t)[\alpha_{j+1}(t) - \alpha_{j+1}^0]}{m_\sigma^2 \tau_{\text{eff}}}, \end{aligned} \quad (20)$$

where $\alpha_j^0 (j = 1, \dots, 4)$ are the coefficients for the equilibrium free energy density $\Omega_0[\sigma]$. Note that different coefficients of the σ field couple with each other in the time-evolution equations. As a result, the terms of σ^i with power $i > 4$ emerge automatically after evolution, even though they vanish at the initial setting. As before, by assuming the contributions from higher power terms are negligible, the free energy is cut off till the fourth order. By setting up the parameters of the dynamical system, we can numerically solve the coupled equations in above, and study the dynamical behaviors of the physical quantities like the cumulants.

5 non-equilibrium cumulants

As we have obtained the time evolution equation (20) of the QCD free energy, we can study the corresponding dynamical cumulants. For simplicity, in the following calculations, we suppose that both the chemical potential and the volume ($V = 10^3 \text{ fm}^3$) are fixed during the time evolution¹. The temperature is assumed to decrease as a function of time:

$$T(t) = T_{\text{ini}} \left(\frac{t + t_{\text{ref}}}{t_{\text{ref}}} \right)^{-\lambda}, \quad (21)$$

where T_{ini} is the initial temperature, $t_{\text{ref}} = 10 \text{ fm}$ is a reference time and the exponent is set to be $\lambda = 0.45$ [31].

¹ With our current setup of the parameters, the time evolution in the critical region is very fast. Hence, the change of the volume during the expansion is neglected. In realistic fireball system, the changing of volume must be included.

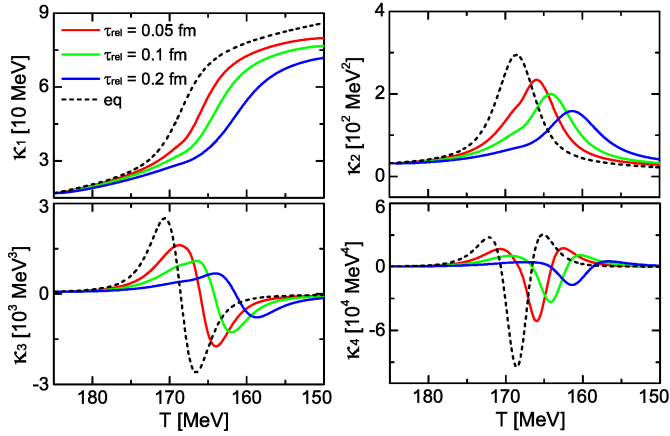


Fig. 4: The non-equilibrium cumulants with respect to the temperature, for different relaxation rates. Here $\mu = 250$ MeV and $V = 10^3$ fm³.

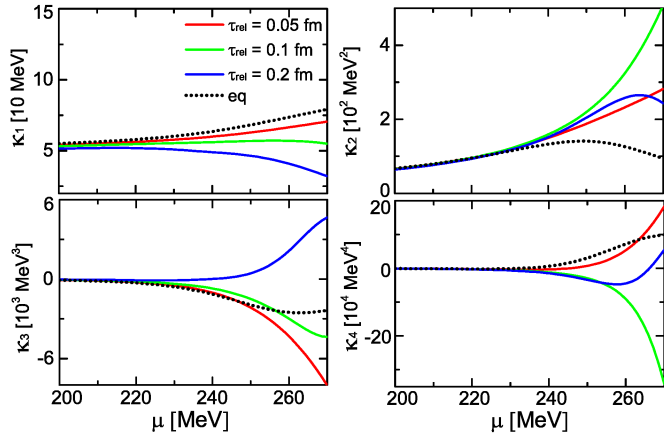


Fig. 5: The non-equilibrium cumulants with respect to the chemical potential on the freeze-out line, for different relaxation rates.

In Fig. 4, we plot the evolution of the cumulants for different relaxation rates, starting from an initial temperature $T_{\text{ini}} = 185$ MeV. The monotonicity of the equilibrium cumulants are exactly memorized by the non-equilibrium cumulants, and reproduced in the later evolution process. As the increase of relaxation rate, the peaks and dips of the non-equilibrium cumulants are suppressed, and the typical structure for each order of the cumulants appears in a later time. Note that in the current finite size system, the memory effects shown in Fig. 4 is similar for different chemical potentials for both the crossover and the first order phase transition cases.

Next, we study the dynamical result of the σ 's cumulants at a hypothetical freeze-out line. The initial temperature and the hypothetical freeze-out temperature are supposed to be about 5.05 MeV above and 3.37 MeV below the phase transition temperature, respectively (i.e. $\eta_1 = 1.5 \times 10^5$ MeV³ for the initial state and $\eta_1 = -1.0 \times 10^5$ MeV³ for the final state, marked as blue and red lines in the bottom-right subfigure in Fig. 3). In Fig. 5 we present the non-equilibrium cumulants with respect to the chemical potential. With different relaxation rates, the

non-equilibrium cumulants at large chemical potentials (mainly on the first order side) significantly deviate from the equilibrium cumulants, and develop rich structures. Especially, for the blue line with $\tau_{\text{rel}} = 0.2$ fm, κ_3 change its sign, and κ_4 presents non-monotonic behaviors compared to the equilibrium ones. These rich structures are suggestive for the understanding of the STAR data [27].

The dynamical behaviors of the cumulants can be understood from the equilibrium cumulants by considering the memory effects. Let us define an effective freeze-out temperature (for each chemical potential) where the equilibrium expectation of the σ field, κ_1 , equals to the dynamical κ_1 on the freeze-out point. The effective freeze-out lines for different relaxation rates are shown in the bottom-right subfigure of Fig. 3 (The dashed red, green and blue lines). From the equilibrium cumulants κ_2 - κ_4 on the effective freeze-out lines, we can approximately read the sign of the non-equilibrium cumulants in Fig. 5. Specifically, for κ_3 , when the relaxation rate is large, say $\tau_{\text{rel}} = 0.2$ fm, the effective freeze-out line in the crossover region is basically at the left side of the phase transition line ($\eta_1 < 0$), while in the first order phase transition region, it is still at the right side of the phase transition line ($\eta_1 > 0$), leading to a positive dynamical κ_3 (see κ_3 in Fig. 3). For κ_4 , when $\tau_{\text{rel}} = 0.1$ fm, the effective freeze-out line falls into the negative κ_4 region; when $\tau_{\text{rel}} = 0.2$ fm ($\tau_{\text{rel}} = 0.05$ fm), the effective freeze-out line crosses the right sign-change line of the κ_4 in η_1 - η_2 plane (see κ_4 in Fig. 3). In general, the memory effects in the first order phase transition region is more significant than that in the crossover region (i.e. the cumulants record earlier information at larger μ), which is because in the first order phase transition region, the barrier in the free energy strongly delays the dynamical evolution of the σ field.

6 Discussion

In summary, we parameterize the Landau free energy of the χ PT by mapping it to the Ising free energy. With the parametric free energy, we study the equilibrium cumulants in a finite size system. The volume of the system significantly influences the fluctuations of the σ field. In the equilibrium case, we find that for a typical QGP fireball size with volume $V = 10^3$ fm³, the probability distribution of the σ field is broadened near the phase transition line, leading to enhancements of the fluctuations and rounding of the discontinuities on the first order phase transition side. Moreover, the fourth order cumulant κ_4 of the σ field is universally negative in the phase transition region on both the crossover and the first order phase transition side. Compared to the crossover region, all cumulants in the first order phase transition region are enhanced, due to the two-peak shape of σ 's distribution in the finite system (where the barrier of the free energy density is of the order of T/V). Utilizing the Fokker-Plank equation, we derive the real-time evolution of the parametric free energy, and further, by setting the cooling down process of the system, we analyze the time evolution of non-equilibrium cumulants at different phase transition scenarios and non-equilibrium cumulants on the hypothetical freeze-out line. We find that earlier information about the cumulants are recorded in the first order phase transition region, compared to the crossover region. Like the earlier studies, the dynamical

cumulants can be different from the equilibrium ones from both the magnitude and the sign, and can be nonmonotonic on the hypothetical freeze-out line.

Note that in our study, we adopt the zero mode approximation which assumes the order parameter is uniform in space. The nonzero modes can be further taken into account if one employs the Ginzburg-Landau free energy. Moreover, due to the flexibility of our parameterization, the parametric free energy and its dynamical evolution can be easily combined with a realistic dynamical model (like that in chiral hydrodynamics [38, 39, 40, 41] or Hydro+ [42]), to study the full dynamical process with phase transition.

Now compare our method with the former studies on the non-equilibrium cumulants in Refs. [31, 32, 33, 34]. In Ref. [31], they presented pioneering studies on the real-time evolution of non-Gaussian cumulants derived from the Fokker-Plank equation. The QCD equation of state near the critical point in the thermodynamic limit is inspired from the Ising model and the parameterization is realized by linearly mapping QCD variables (μ, T) to the Ising variables (r, h). The resulted equation of state and the corresponding equilibrium cumulants could contain the quantum correction from the fluctuations of the order parameter. However, the volume effects on the equation of state and cumulants are fully omitted, which is valid when the correlation length is significantly smaller than the size of the system. In this case, the discontinuities of the equilibrium distribution function of the σ field hinder the simulation of critical dynamics with the Fokker-Plank equation in the first order phase transition region, which assumes the slight deviations of dynamical probability distribution from the equilibrium one. As shown in our study, when the size is small enough, the finite size effects becomes significant especially in the first order phase transition region. The rounding effects justifies the application of the Fokker-Plank equation in the first order phase transition region. In Refs. [32, 33, 34], the dynamical evolution of cumulants on different phase transition scenarios were studied based on event-by-event simulations of Langevin equation. The effective potential of σ is obtained by evaluating the linear sigma model. The evolution takes account of the fluctuation effects (long wavelength modes) in the real space. However, the shortcoming of this approach is the location of the critical point is fixed by the model parameters of the linear sigma model, which is even far below the chemical freeze-out line determined by the statistical model and experimental data. Thus the dynamical equations of the critical fluctuations in Ref. [32, 33] could not be combined with the hydrodynamic equations, and describe the realistic experimental process. In recent studies, the parameterization of QCD equation of state with non-linear corrections (consistent with the lattice results) have been extended from the critical region to a broader region in the μ - T plane [50, 51, 52]. Similar further extension of the parameterization of the free energy density will be important for studying the dynamic evolution of critical fluctuations at RHIC.

Acknowledgments

Jiang thanks Volodymyr Vovchenko, and Huichao Song for discussion and comments, and Frankfurt Institute for Advanced Studies at Frankfurt am Main for hospitality, where part of this

work has been done. Jiang acknowledges the support from the NSFC under grant no. 12105223, Stöcker acknowledges the support from the Walter Greiner Gesellschaft zur Förderung der physikalischen Grundlagenforschung e.V. through the Judah M. Eisenberg Laureatus Chair at Goethe Universität, and Zheng acknowledges the support from the NSFC under grant no. 12175180 and the research start-up funding from Northwest University.

References

1. N. Cabibbo and G. Parisi, Exponential hadronic spectrum and quark liberation, *Phys. Lett. B* **59**, 67 (1975).
2. A. M. Halasz, A. D. Jackson, R. E. Shrock, M. A. Stephanov, and J. J. M. Verbaarschot, On the phase diagram of QCD, *Phys. Rev. D* **58**, 096007 (1998).
3. G. Baym, Ultrarelativistic heavy ion collisions: the first billion seconds, *Nucl. Phys. A* **956**, 1 (2016).
4. K. Fukushima and T. Hatsuda, The phase diagram of dense QCD, *Rep. Prog. Phys.* **74**, 014001 (2011).
5. M. M. Aggarwal *et al.* [STAR Collaboration], An experimental exploration of the QCD phase diagram: the search for the critical point and the onset of de-confinement, [arXiv:1007.2613](https://arxiv.org/abs/1007.2613) (2010).
6. The DOE/NSF Nuclear Science Advisory Committee, The frontiers of nuclear science, a long range plan, [arXiv:0809.3137](https://arxiv.org/abs/0809.3137) (2008).
7. H. Stöcker and W. Greiner, High energy heavy ion collisions — probing the equation of state of highly excited hadronic matter, *Phys. Repts.* **137**, 277 (1986).
8. T. Hatsuda and T. Kunihiro, Fluctuation effects in hot quark matter: Precursors of chiral transition at finite temperature, *Phys. Rev. Lett.* **55**, 158 (1985).
9. T. D. Lee and G. C. Wick, Vacuum stability and vacuum excitation in a spin-0 field theory, *Phys. Rev. D*, **9**, 2291 (1974).
10. F. R. Brown, *et al.*, On the existence of a phase transition for QCD with three light quarks, *Phys. Rev. Lett.* **65**, 2491 (1990).
11. Y. Aoki, G. Endrodi, Z. Fodor, S. D. Katz, and K. K. Szabó, The order of the quantum chromodynamics transition predicted by the standard model of particle physics, *Nature* **443**, 675 (2006).
12. Y. Aoki, S. Borsányi, S. Dürr, Z. Fodor, S. D. Katz, S. Krieg, and K. K. Szabo, The QCD transition temperature: results with physical masses in the continuum limit II, *JHEP* **0906**, 088 (2009).
13. F. Karsch and E. Laermann, Thermodynamics and in-medium hadron properties from lattice QCD, *Quark gluon plasma* **3**, 1 (2004) (Edited by R.C. Hwa, and X.-N. Wang); [hep-lat/0305025](https://arxiv.org/abs/hep-lat/0305025) (2003).
14. S. P. Klevansky, The Nambu-Jona-Lasinio model of quantum chromodynamics, *Rev. Mod. Phys.* **64**, 649 (1992).
15. K. Fukushima, Chiral effective model with the Polyakov loop, *Phys. Lett. B* **591**, 277 (2004).
16. W. J. Fu, Z. Zhang, and Y. X. Liu, 2+1 flavor Polyakov-Nambu-Jona-Lasinio model at finite temperature and nonzero chemical potential, *Phys. Rev. D* **77**, 014006 (2008).
17. L. J. Jiang, X. Y. Xin, K. L. Wang, S. X. Qin, and Y. X. Liu, Revisiting the phase diagram of the three-flavor quark system in the Nambu-Jona-Lasinio model, *Phys. Rev. D* **88**, 016008 (2013).
18. B.-J. Schaefer and J. Wambach, The phase diagram of the quark meson model, *Nucl. Phys. A* **757**, 479 (2005).
19. B.-J. Schaefer, J. M. Pawłowski, and J. Wambach, Phase structure of the Polyakov-quark-meson model, *Phys. Rev. D* **76**, 074023 (2007).

20. T. K. Herbst, J. M. Pawłowski, and B.-J. Schaefer, The phase structure of the Polyakov-quark-meson model beyond mean field, *Phys. Lett. B* **696**, 58 (2011).
21. J. Berges, N. Tetradis, and C. Wetterich, Non-perturbative renormalization flow in quantum field theory and statistical physics, *Phys. Rept.* **363**, 223 (2002).
22. C. D. Roberts and A. G. Williams, Dyson-Schwinger equations and their application to hadronic physics, *Prog. Part. Nucl. Phys.* **33**, 477 (1994).
23. S. X. Qin, L. Chang, H. Chen, Y. X. Liu, and C. D. Roberts, Phase diagram and critical end point for strongly interacting quarks, *Phys. Rev. Lett.* **106**, 172301 (2011).
24. M. A. Stephanov, Non-Gaussian fluctuations near the QCD critical point, *Phys. Rev. Lett.* **102**, 032301 (2009).
25. C. Athanasiou, K. Rajagopal, and M. Stephanov, Using higher moments of fluctuations and their ratios in the search for the QCD critical point, *Phys. Rev. D* **82**, 074008 (2010).
26. L. Adamczyk *et al.* [STAR Collaboration], Energy dependence of moments of net-proton multiplicity distributions at RHIC, *Phys. Rev. Lett.* **112**, 032302 (2014).
27. X. Luo [STAR Collaboration], Energy dependence of moments of net-proton and net-charge multiplicity distributions at STAR, *PoS CPOD* **2014**, 019 (2014).
28. J. Adam *et al.* [STAR Collaboration], Nonmonotonic energy dependence of net-proton number fluctuations, *Phys. Rev. Lett.* **126**, 092301 (2021).
29. L. Jiang, P. Li, and H. Song, Correlated fluctuations near the QCD critical point, *Phys. Rev. C* **94**, 024918 (2016).
30. M. A. Stephanov, Evolution of fluctuations near QCD critical point, *Phys. Rev. D* **81**, 054012 (2010).
31. S. Mukherjee, R. Venugopalan, and Y. Yin, Real-time evolution of non-Gaussian cumulants in the QCD critical regime, *Phys. Rev. C* **92**, 034912 (2015).
32. L. Jiang, S. Wu, and H. Song, Dynamical fluctuations in critical regime and across the 1st order phase transition, *Nucl. Phys. A* **967**, 441 (2017).
33. L. Jiang, S. Wu, and H. Song, Enhancements of high order cumulants across the 1st order phase transition boundary, *EPJ Web Conf.* **171**, 16003 (2018).
34. L. Jiang and J. Chao, Non-equilibrium cumulants within model A near the QCD critical point, *arXiv:2112.04667* (2021).
35. M. Sakaida, M. Asakawa, H. Fujii, and M. Kitazawa, Dynamical evolution of critical fluctuations and its observation in heavy ion collisions, *Phys. Rev. C* **95**, 064905 (2017).
36. M. Nahrgang, M. Bluhm, T. Schaefer, and S. A. Bass, Diffusive dynamics of critical fluctuations near the QCD critical point, *Phys. Rev. D* **99**, 116015 (2019).
37. K. Paech, H. Stöcker, and A. Dumitru, Hydrodynamics near a chiral critical point, *Phys. Rev. C* **68**, 044907 (2003).
38. M. Nahrgang, S. Leupold, C. Herold, and M. Bleicher, Nonequilibrium chiral fluid dynamics including dissipation and noise, *Phys. Rev. C* **84**, 024912 (2011).
39. M. Nahrgang, C. Herold, S. Leupold, I. Mishustin, and M. Bleicher, The impact of dissipation and noise on fluctuations in chiral fluid dynamics, *J. Phys. G* **40**, 055108 (2013).
40. C. Herold, M. Nahrgang, I. Mishustin, and M. Bleicher, Chiral fluid dynamics with explicit propagation of the Polyakov loop, *Phys. Rev. C* **87**, 014907 (2013).
41. C. Herold, M. Nahrgang, I. Mishustin and M. Bleicher, Formation of droplets with high baryon density at the QCD phase transition in expanding matter, *Nucl. Phys. A* **925**, 14 (2014).
42. M. Stephanov and Y. Yin, Hydrodynamics with parametric slowing down and fluctuations near the critical point, *Phys. Rev. D* **98**, 036006 (2018).
43. K. Rajagopal, G. Ridgway, R. Weller and Y. Yin, Understanding the out-of-equilibrium dynamics near a critical point in the QCD phase diagram, *Phys. Rev. D* **102**, 094025 (2020).
44. L. Du, U. Heinz, K. Rajagopal, and Y. Yin, Fluctuation dynamics near the QCD critical point, *Phys. Rev. C* **102**, 054911 (2020).
45. X. An, G. Başar, M. Stephanov, and H. U. Yee, Evolution of Non-Gaussian Hydrodynamic Fluctuations, *Phys. Rev. Lett.* **127**, 072301 (2021).
46. J.-H. Zheng and L. Jiang, Nonuniform-temperature effects on the phase transition in an Ising-like model, *Phys. Rev. D* **104**, 016031 (2021).
47. M. Bluhm, M. Nahrgang, S. A. Bass, and T. Schaefer, Impact of resonance decays on critical point signals in net-proton fluctuations, *Eur. Phys. J. C* **77**, 210 (2017).
48. M. Pradeep, K. Rajagopal, M. Stephanov, and Y. Yin, Freezing out gluons in Hydro+ near the QCD critical point, *Phys. Rev. D* **106**, 036017 (2022).
49. D. Mroczek, A. R. Nava Acuna, J. Noronha-Hostler, P. Parotto, C. Ratti, and M. A. Stephanov, Quartic cumulant of baryon number in the presence of a QCD critical point, *Phys. Rev. C* **103**, 034901 (2021).
50. A. Monnai, B. Schenke, and C. Shen, Equation of state at finite densities for QCD matter in nuclear collisions, *Phys. Rev. C* **100**, 024907 (2019).
51. J. Noronha-Hostler, P. Parotto, C. Ratti, and J. M. Stafford, Lattice-based equation of state at finite baryon number, electric charge and strangeness chemical potentials, *Phys. Rev. C* **100**, 064910 (2019).
52. P. Parotto, M. Bluhm, D. Mroczek, M. Nahrgang, J. Noronha-Hostler, K. Rajagopal, C. Ratti, T. Schäfer, and M. Stephanov, QCD equation of state matched to lattice data and exhibiting a critical point singularity, *Phys. Rev. C* **101**, 034901 (2020).
53. S. Gavin, A. Gocksch and R. D. Pisarski, QCD and the chiral critical point, *Phys. Rev. D* **49**, R3079 (1994).
54. R. Guida and J. Zinn-Justin, 3D Ising model: the scaling equation of state, *Nucl. Phys. B* **489**, 626 (1997).
55. B. Berdnikov and K. Rajagopal, Slowing out of equilibrium near the QCD critical point, *Phys. Rev. D* **61**, 105017 (2000).
56. C. Nonaka and M. Asakawa, Hydrodynamical evolution near the QCD critical end point, *Phys. Rev. C* **71**, 044904 (2005).
57. M. A. Stephanov, Sign of Kurtosis near the QCD Critical Point, *Phys. Rev. Lett.* **107**, 052301 (2011).
58. S. Mukherjee, R. Venugopalan and Y. Yin, Universal off-equilibrium scaling of critical cumulants in the QCD phase diagram, *Phys. Rev. Lett.* **117**, 222301 (2016).
59. R. D. Pisarski and F. Wilczek, Remarks on the chiral phase transition in chromodynamics, *Phys. Rev. D* **29**, 338(R) (1984).
60. M. Gell-Mann and M. Lévy, The axial vector current in beta decay, *Nuovo Cimento* **16**, 705 (1960).
61. N. Petropoulos, Linear sigma model and chiral symmetry at finite temperature, *J. Phys. G: Nuclear and Particle Physics* **25**, 2225 (1999).
62. V. Vovchenko, D. V. Anchishkin, M. I. Gorenstein and R. V. Poberezhnyuk, Scaled variance, skewness, and kurtosis near the critical point of nuclear matter, *Phys. Rev. C* **92**, 054901 (2015).
63. V. Vovchenko, M. I. Gorenstein and H. Stoecker, van der Waals interactions in hadron resonance gas: from nuclear matter to lattice QCD, *Phys. Rev. Lett.* **118**, 182301 (2017).
64. E. Brezin and J. Zinn-Justin, Finite size effects in phase transitions, *Nucl. Phys. B* **257**, 867 (1985).
65. Y. Imry, Finite-size rounding of a first-order phase transition, *Phys. Rev. B* **21**, 2042 (1980).

- 66. C. Spieles, H. Stöcker and C. Greiner, Phase transition of a finite quark-gluon plasma, [Phys. Rev. C **57**, 908 \(1998\)](#).
- 67. E. E. Zabrodin, L.V. Bravina, H. Stöcker and W. Greiner, Homogeneous nucleation of quark-gluon plasma, finite size effects, and long-lived metastable objects, [Phys. Rev. C **59**, 894 \(1999\)](#).
- 68. P. C. Hohenberg, and B. I. Halperin, Theory of dynamic critical phenomena, [Rev. Mod. Phys. **49**, 435 \(1977\)](#).
- 69. D. T. Son and M. A. Stephanov, Dynamic universality class of the QCD critical point, [Phys. Rev. D **70**, 056001 \(2004\)](#).